SEDIMENTOLOGY the journal of the International Association of Sedimentologists

Sedimentology (2020) **67**, 951–970 doi: 10.1111/sed.12668

Mega-monsoon variability during the late Triassic: Re-assessing the role of orbital forcing in the deposition of playa sediments in the Germanic Basin

ANDRÉ BAHR*, GILLES KOLBER*, STEFANIE KABOTH-BAHR*†[1], LUTZ REINHARDT‡, OLIVER FRIEDRICH* and JÖRG PROSS*

**Institute of Earth Sciences, Heidelberg University, Im Neuenheimer Feld 234–236, 69120 Heidelberg, Germany (E-mail: andre.bahr@geow.uni-heidelberg.de)*

†Department of Geosciences, National Taiwan University, Roosevelt Road, 106 Taipei, Taiwan

‡Federal Institute for Geosciences and Natural Resources, Stilleweg 2, 30655 Hannover, Germany

Associate Editor – Ola Kwiecien

ABSTRACT

The formation of the supercontinent Pangaea during the Permo–Triassic gave rise to an extreme monsoonal climate (often termed 'mega-monsoon') that has been documented by numerous palaeo-records. However, considerable debate exists about the role of orbital forcing in causing humid intervals in an otherwise arid climate. To shed new light on the forcing of monsoonal variability in subtropical Pangaea, this study focuses on sediment facies and colour variability of playa and alluvial fan deposits in an outcrop from the late Carnian (*ca* 225 Ma) in the southern Germanic Basin, south-western Germany. The sediments were deposited against a background of increasingly arid conditions following the humid Carnian Pluvial Event (*ca* 234 to 232 Ma). The *ca* 2·4 Myr long sedimentary succession studied shows a tripartite long-term evolution, starting with a distal mud-flat facies deposited under arid conditions. This phase was followed by a highly variable playa-lake environment that documents more humid conditions and finally a regression of the playa-lake due to a return of arid conditions. The red–green (a^*) and lightness (L^*) records show that this long-term variability was overprinted by alternating wet/dry cycles driven by orbital precession and *ca* 405 kyr eccentricity, without significant influence of obliquity. The absence of obliquity in this record indicates that high-latitude forcing played only a minor role in the southern Germanic Basin during the late Carnian. This is different from the subsequent Norian when high-latitude signals became more pronounced, potentially related to the northward drift of the Germanic Basin. The recurring pattern of pluvial events during the late Triassic demonstrates that orbital forcing, in particular eccentricity, stimulated the occurrence and intensity of wet phases. It also highlights the possibility that the Carnian Pluvial Event, although most likely triggered by enhanced volcanic activity, may also have been modified by an orbital stimulus.

Keywords Carnian Pluvial Event, Germanic Basin, Late Triassic, mega-monsoon, orbital forcing, playa-lake.

[1]Present address: Institute of Geosciences, University of Potsdam, Karl-Liebknecht-Str. 24-25, 14476 Potsdam-Golm, Germany

[Correction added on 15 October 2020 after first publication: Copyright line of this article was changed and Projekt Deal funding statement has been added in acknowledgements section.]

INTRODUCTION

The formation of the supercontinent Pangaea during the Permo–Triassic led to a distinct global configuration of an azonal climate pattern with a dominance of monsoonal wind systems in (sub)tropical latitudes (Parrish & Peterson, 1988; Kutzbach & Gallimore, 1989; Sellwood & Valdes, 2006) that caused the alternating occurrence of extreme wet and dry seasons over Pangaea (Parrish & Peterson, 1988; Dubiel *et al.*, 1991; Mutti & Weissert, 1995). The development of this 'mega-monsoon' originated from the strong warming of Laurasia (Northern Hemisphere) relative to Gondwana (Southern Hemisphere) during boreal summer and *vice versa* (Kutzbach & Gallimore, 1989; Kutzbach, 1994). These steep interhemispheric continental temperature contrasts led to a strong pressure gradient that in turn caused vigorous northward air flow. During boreal winter, the pressure gradient and subsequent air flow was reversed, causing intensified precipitation over Gondwana; meanwhile, dry conditions prevailed over Laurasia (Kutzbach & Gallimore, 1989; Sellwood & Valdes, 2006). Whilst crossing the warm Tethys, these air masses were charged with moisture before being advected into the interior of Laurasia or Gondwana, respectively, where they caused strong rainfall in the respective summer seasons (Parrish & Peterson, 1988; Dubiel *et al.*, 1991). The strong expression of the Triassic mega-monsoon was further promoted by high atmospheric greenhouse-gas concentrations with atmospheric pCO_2 levels of 2000 to 3550 ppm (Tanner *et al.*, 2001; Retallack, 2002; Kidder & Worsley, 2004). These high pCO_2 concentrations impacted the radiative forcing, thereby increasing the land–ocean temperature contrast that drives monsoonal wind systems (Lee & Wang, 2014; Mohtadi *et al.*, 2016; Wang *et al.*, 2017).

Based on proxy information from marine and terrestrial archives, the maximum intensity of the Pangaean 'mega-monsoon' was reached during the mid-Carnian (Robinson, 1973; Wang, 2009), resulting in the so-called 'Carnian Pluvial Event' (*ca* 234 to 232 Ma; Bernardi *et al.*, 2018) with a rather brief duration of *ca* 1·0 to 1·2 Myr (Miller *et al.*, 2017; Bernardi *et al.*, 2018; Dal Corso *et al.*, 2018). The Carnian Pluvial Event was apparently a quasi-global phenomenon, because evidence for humid conditions is available from both low-latitude and high-latitude settings. In the Germanic Basin of Central Europe (Fig. 1) this humid phase is represented by the widespread, fluvial 'Schilfsandstein' (Stuttgart Formation; Aigner & Bachmann, 1992; Hornung & Brandner, 2005; Ogg, 2015; Fig. 2). Other examples include Kotel'nyi Island in Siberia, where increased rainfall and fluvial input are registered (Bragin *et al.*, 2012), as well as the Yangtze Platform (Zhang *et al.*, 2015) and Spiti in the Himalayas (Hornung *et al.*, 2007), where carbonate sedimentation was terminated by increased siliciclastic influx. During the subsequent Norian, a gradual aridification trend developed across Pangaea that became most evident during the middle Norian at *ca* 215 Ma (Nordt *et al.*, 2015). The reason behind this aridification trend is still controversially debated. While some authors argue that it may have at least partially resulted from the plate-tectonic drift of formerly tropical sites into the subtropics or mid-latitudes (Kent & Tauxe, 2005; Kent *et al.*, 2014), others argue that regional orogenic effects may also have played a role in initiating the demise of humid conditions (Nordt *et al.*, 2015). The relatively arid late Norian was followed by a return to more humid conditions in the Rhaetian (Berra *et al.*, 2010; Mazza *et al.*, 2010; McKie, 2014).

The origin of the Carnian Pluvial Event is still a matter of debate. It is most commonly attributed to volcanic CO_2 degassing from the Wrangellia Large Igneous Province in concert with the destabilization of clathrates; such a scenario could readily explain the negative carbon isotope excursions that occur during the Carnian Pluvial Event (Furin *et al.*, 2006; Miller *et al.*, 2017; Dal Corso *et al.*, 2018). Other explanations involve the uplift of Fennoscandia (Hornung & Brandner, 2005; Arche & López-Gómez, 2014) which modified large-scale atmospheric circulation patterns and led to an intensification of monsoonal rainfall, particularly in the Germanic Basin.

Although the global expression of the Pangaean mega-monsoon is well-documented by proxy (Nairn & Smithwick, 1976; Parrish, 1993; Preto *et al.*, 2010; Tanner, 2018) and model evidence (Kutzbach & Gallimore, 1989; Sellwood & Valdes, 2006), uncertainties have remained about the degree to which orbital forcing has influenced Pangaean climate. This ultimately raises the question of whether – and, if yes, to what extent – Milankovitch cyclicities were largely overprinted by autocyclical processes and/or tectonic activity (Mertz & Hubert, 1990; Kozur & Bachmann, 2010; Tanner, 2010; Arche & López-Gómez, 2014). In particular, the role of

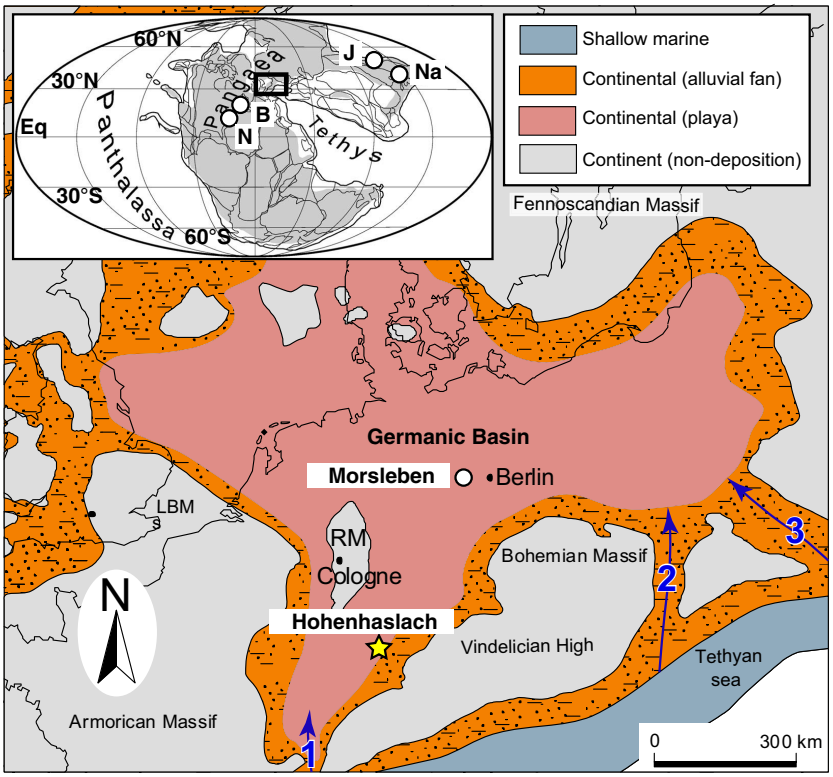

Fig. 1. Palaeogeographic map of the Germanic Basin during the Carnian (modified after Ziegler, 1990, and Vollmer, 2005). Marine ingressions from the Tethys through the Burgundian (1), Silesian (2) and Carpathian (3); gates are indicated by blue arrows; LBM – London–Brabant Massif, RM – Rhenish Massif. Inset map shows global palaeogeographic configuration during the late Triassic (after Scotese, 2004). The maps include the location of the Hohenhaslach section within the Stromberg Trough (yellow star) and locations cited in the text (white circles; B – Blomidon Basin, J –Junggar Basin, N – Newark Basin, Na – Nanpanjiang Basin).

obliquity forcing on the mega-monsoon under late Triassic boundary conditions has remained poorly understood. Since the influence of precession and eccentricity is intrinsic to low-latitude climate systems such as the monsoon (Kutzbach & Liu, 1997; Mohtadi *et al.*, 2016; Wang *et al.*, 2017), the recognition of obliquity-related cyclicity in recent monsoonal systems (Lourens *et al.*, 1996, 2001; Bosmans *et al.*, 2015a,b) is astounding. An obliquity influence on monsoonal systems is unexpected because the direct influence of obliquity variations on solar irradiation in the low latitudes is negligible (Laskar *et al.*, 2004). One concept to explain the expression of obliquity in present monsoonal systems invokes an intensified interhemispheric insolation and temperature gradient during maximum obliquity; numerical simulations of the African monsoonal system suggest that such a strong temperature gradient enhances the northward moisture transport and feeds monsoonal rainfall in the Northern Hemisphere (Bosmans *et al.*, 2015a,b). Triassic low-latitude records of monsoonal variability with obliquity imprint have indeed been reported from, for example, the Blomidon Formation in the Fundy Basin of Nova Scotia (Mertz & Hubert, 1990; Kent & Olsen, 2000), the Hubei Province in Southern China (Wu *et al.*, 2012; Li *et al.*, 2016a,b), and the Germanic Basin (Reinhardt, 2000; Reinhardt & Ricken, 2000; Vollmer *et al.*, 2008) (for locations see Fig. 1). On the other hand, the imprint of obliquity on sedimentary cycles has been debated for the tropical deposits of the Newark Basin (Olsen, 1986; Kent & Olsen, 2000; Kent *et al.*, 2017). This raises the question of whether obliquity generally exerted control on the (late) Triassic mega-monsoon or whether obliquity influence was merely a regional-scale phenomenon.

To shed new light on the role of orbital forcing within the Pangaean mega-monsoon system, this study has analysed the depositional dynamics of alluvial fan/playa deposits of late Triassic (Keuper) sediments from the southern Germanic Basin. The sediments studied derive from the Stromberg Trough in south-western Germany (Fig. 1), a sub-basin of the Germanic Basin with an extended and well-preserved section of upper Triassic strata. The palaeogeographic setting of the Stromberg Trough is located within *ca* 250 km distance to the shoreline of the Tethys (Ziegler, 1990), the major moisture source for monsoonal rainfall, making the region ideally suited for palaeoclimate studies focusing on monsoon dynamics. To investigate potential

orbital control on late Triassic sedimentation in the Stromberg Trough, high-resolution sediment colour profiles have been obtained and advanced statistical procedures applied that allow for a robust assessment of potential orbital cycles.

GEOLOGICAL SETTING AND STRATIGRAPHIC FRAMEWORK

The Germanic Basin evolved after the end of the Variscan Orogeny as a largely flat intracontinental basin with most of its sedimentary filling being deposited during the Permian and the Mesozoic. During the late Triassic, it stretched from subtropical to lower mid-latitudes; it was bordered by the Vindelician High in the south-east, the Bohemian Massif in the east, and the massifs of London–Brabant and Armorica in the west and north-west (Ziegler, 1990; Fig. 1). The Stromberg Trough is a geological sub-structure within the south-western part of the Germanic Basin. Located at the western border of the Vindelician High, it has a surface area of *ca* 500 km^2 (Carlé & Linck, 1949; Fig. 1). The oldest strata of the Stromberg Trough belong to the middle Triassic (Anisian) Muschelkalk Formation [LGRB (Landesamt für Geologie, Rohstoffe und Bergbau), 2000; Fig. 2). They consist of marly limestones intercalated with evaporites that formed in an epicontinental setting as a result of cyclic marine ingressions into the Germanic Basin through the Burgundian, Carpathian and Silesian gates (Kozur & Bachmann, 2010; Fischer *et al.*, 2012). Following the terminal regression of the Muschelkalk sea during the middle Triassic (Ladinian), terrestrial clastic sediments of the subsequent late Triassic 'Keuper' were deposited in the southern and central part of the Germanic Basin. They consist of repeated alternations of marine-influenced deltaic to brackish and terrestrial limnic to playa-lake deposits intercalated with terminal alluvial fans (LGRB, 2001) derived from the bordering Vindelician High, resulting in an up to 1 km thick sedimentary succession (Boigk *et al.*, 1974) deposited between the early Ladinian and the end of the Rhaetian (Gradstein *et al.*, 2012).

Within the up to 440 m thick succession of late Triassic strata (Keuper, k) in the Stromberg Trough (LGRB, 2000, 2001), the Mainhardt Formation (kmMh) comprises a 30 to 40 m thick series of partially gypsiferous, multi-coloured clays and dolomites representing playa-lake and distal alluvial plain-type environments (LGRB, 2001; Heunisch & Nitsch, 2011) of the Middle Keuper (km). Intercalated arcose-type sandstones represent alluvial fan deposits (Geyer *et al.*, 2011). The Mainhardt Formation is unconformably overlain by fluviatile sandstones and clays of the Löwenstein Formation (kmLw; formerly termed 'Stubensandstein'; Fig. 2) that were deposited in a more humid environment than the Mainhardt Formation (Kozur & Bachmann, 2010; Bachmann & Kozur, 2015). Further details of the geological units of the late Triassic

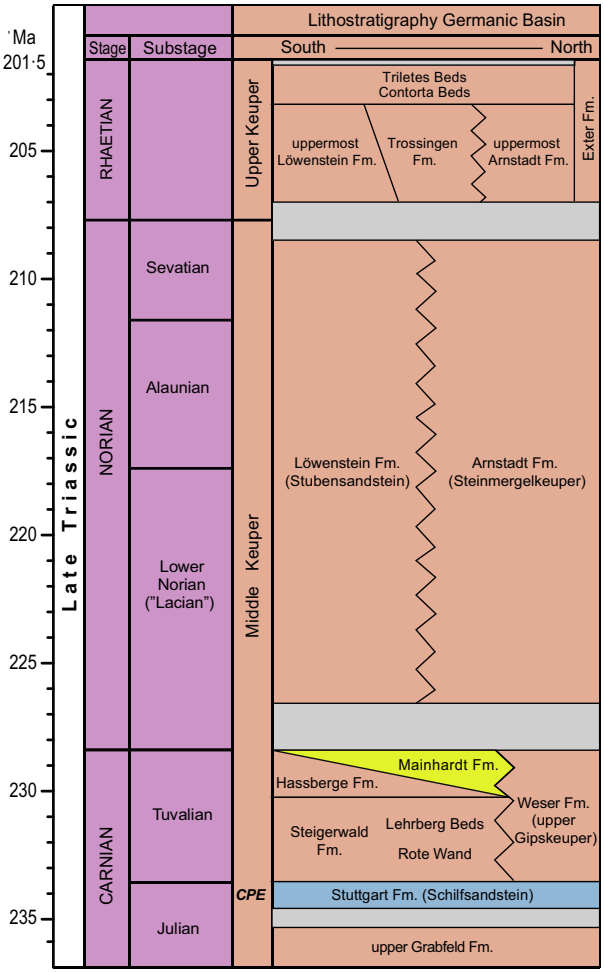

Fig. 2. Stratigraphy of the late Triassic in the Germanic Basin with the studied Mainhardt Formation highlighted, following the stratigraphy of the late Triassic after Kent *et al.* (2017). Note that the Carnian Pluvial Event (CPE) is associated with the 'Stuttgart Formation' (marked in blue; Aigner & Bachmann, 1992; Hornung & Brandner, 2005; Ogg, 2015). Grey intervals denote major hiatuses. Note that the absolute duration of the stratigraphic gaps is yet poorly constrained, but widely considered minor (Franz *et al.*, 2018).

in the southern Germanic Basin, including synonyms of geological units and outdated local names can be found in LGRB (2016).

The stratigraphic position of the Mainhardt Formation has been previously constrained through palynological evidence to the latest Carnian (Tuvalian) (Heunisch & Nitsch, 2011), which is in line with stratigraphic evidence from conchostracans (Kozur & Bachmann, 2005). However, the playa sediments likely record only part of this sub-stage because neither the Carnian/Norian boundary nor the underlying Tuvalian/Julian sub-stage boundary could yet be identified in the region (Heunisch & Nitsch, 2011; Nitsch, 2018).

PREVIOUS EVIDENCE FOR ORBITAL FORCING ON SEDIMENTATION IN THE GERMANIC BASIN

Cyclical sedimentation patterns have been found in several sections of the Germanic Triassic, including the largely terrestrial formations of the Buntsandstein (Geluk & Röhling, 1997; Szurlies, 2004, 2007) and Keuper (Aigner & Bachmann, 1989; Reinhardt, 2000; Reinhardt & Ricken, 2000; Vollmer, 2005; Vollmer *et al.*, 2008; Nitsch, 2018) as well as the marine Muschelkalk (Kedzierski, 2000; Götz, 2002; Götz & Wertel, 2002). Commonly, the cyclicity observed in the terrestrial settings of the Buntsandstein and Keuper has been interpreted to reflect water availability, a direct result of changes in orbitally driven monsoonal rainfall (Kozur & Bachmann, 2005; Bachmann & Kozur, 2015).

In case of the playa-type setting of the Keuper in the Germanic Basin, orbital precession has been invoked as the main driver of cyclical facies successions, interpreted to reflect changes in the precipitation–evaporation balance (Fig. 3; Reinhardt, 2000; Reinhardt & Ricken, 2000; Vollmer, 2005; Vollmer *et al.*, 2008). For the interpretation of the facies succession at the studied section the conceptual model put forward by these authors is followed here (Fig. 3), which is briefly summarized in the following: A playa-lake was established during peak monsoonal intensity when Northern Hemisphere summer insolation reached its maximum during minimum precession. During this phase, clayey, dark grey mudstones (Facies A in Fig. 2) were deposited. Through the subsequent transition of the equinoxes through perihelion, monsoonal rainfall weakened. As a consequence, the lake level decreased and evaporitic dolomite layers formed (Facies B; Fig. 3). This trend to drier conditions culminated through the following summer insolation minimum (and precession maximum) when the playa-lake dried out completely and exposed the sediment to oxidation, which resulted in the deposition of reddish clay (Facies C; Fig. 3). Over the course of the subsequent increase of summer insolation, summer rainfall intensified. As a consequence, increasing groundwater levels aided the formation of pedogenic dolomite nodules (dolocrete, Facies D; Fig. 3). The entire sedimentary cycle recommenced when monsoonal activity peaked during the next precessional maximum, causing the playa to re-submerge. Intercalated gypsum layers (Facies E) typically formed in the succession of mudstone, dolomite and gypsum (Facies succession A–B–E) during the evaporative drawdown of the lake when monsoonal intensity became weaker. The orbitally driven changes in water availability are generally well-reflected by the colour of the sediments, as evidenced by the comparison of sediment colour with mineralogical and geochemical data (Reinhardt & Ricken, 2000; Vollmer *et al.*, 2008). Here, greenish sediments represent reducing conditions during intense monsoonal activity with reduced iron phases, while reddish sediments infer oxidizing conditions during dry intervals characterized by the presence of hematite as the dominant oxidized iron phase (Vollmer *et al.*, 2008; Debret *et al.*, 2011; Voigt *et al.*, 2017; Gastaldo *et al.*, 2019).

MATERIAL AND METHODS

To investigate the nature of cyclical sedimentation patterns of the Mainhardt Formation, the colour alternations (red–green variations represented by a^* and lightness by L^*) and sedimentary composition of an outcrop comprising 18·1 m of the Mainhardt Formation were analysed. This outcrop lies within the Stromberg Trough situated *ca* 0·5 km north-east of the village of Hohenhaslach (coordinates: 49°00′21″N; 09°02′06″E) and comprises the longest continuous section of Tuvalian deposits in the southwestern Germanic Basin (Figs 1 and 4).

After detailed lithostratigraphical logging, spectrophotometric analyses were carried out on freshly exposed sediments using a Konica Minolta CM-700d spectrophotometer (Konica Minolta, Tokyo, Japan) combined with a CM-A178 target mask (Ø 8 mm, with plate). In total, 841

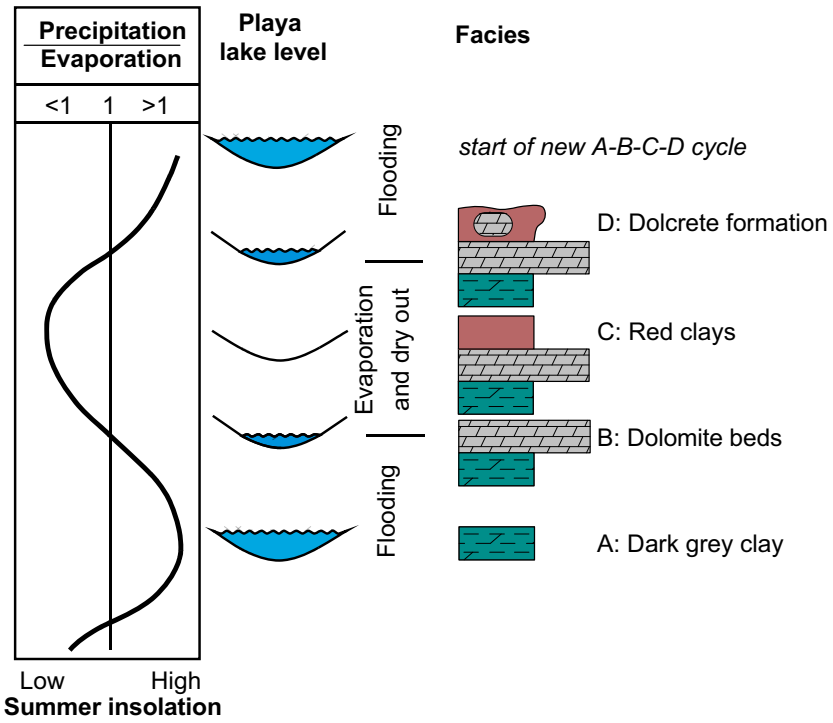

Fig. 3. Evolution of a precession-controlled wet/dry cycle in the upper Triassic of the Germanic Basin (modified after Vollmer, 2005). (A) Maximum Northern Hemisphere summer insolation caused maximum monsoonal rainfall, giving rise to the formation of perennial lakes and the deposition of greyish clays. (B) During equinoxes at perihelion and aphelion, evaporation increased and dolomite beds were formed. (C) Insolation minima resulted in a weaker monsoon, with evaporation exceeding precipitation resulting in the formation of well-oxidized, reddish mudstones. (D) During the subsequent equinox monsoonal activity increased again, leading to a higher groundwater table that caused the formation of pedogenetic dolocrete within the red clays. The next insolation maximum marks the onset of a new cycle.

colour measurements were taken at a spacing of 0·01 to 0·04 m (average: 0·02 m). Colour data is reported in the CIELAB space using the $L^*a^*b^*$ system, which is the most commonly used colour space in sedimentology (Kirby *et al.*, 1999; Piper & Hundert, 2002; Weber *et al.*, 2010; Debret *et al.*, 2011). The $L^*a^*b^*$ system represents a spherical coordinate system with lightness recorded as one axis by L^* with a range from 0 to 100%. The two axes are dimensionless chromaticity variables with values from –60 to +60, with a^* representing the green (negative) to red (positive) axis and b^* the blue (negative) to yellow (positive) axis. To calibrate the spectrophotometer, a Konica Minolta White Calibration Cap CM-A177 and Zero Calibration Box CM-A182 were used. The spectrophotometric data is available in Appendix S1 accompanying this manuscript.

Spectral analysis of the colour data was performed with multitaper method implemented in the 'astrochron' package in R (R Core Team, 2013; Meyers, 2014) on the interpolated and detrended data. Wavelet analysis with a Morlet window was performed using the 'biwavelet' R package (Gouhier *et al.*, 2016). Average Spectral Misfit (ASM) calculations were carried out to assign dominant spectral peaks in the a^* spectrum to orbital frequencies utilizing the 'astrochron' R software package (Meyers, 2014).

RESULTS

Lithology

The outcrop consists of an alternation of greenish, greyish and reddish claystones, with varying portions of intercalated gypsum and dolomite layers (Figs 4 and 5). The interval from the bottom of the studied section up to 7·50 m is dominated by dusky to weakly red, greenish grey and partially mottled claystones. Dolomite beds with thicknesses of up to 0·15 m are intercalated in the greenish-grey claystone at 2·06 m,

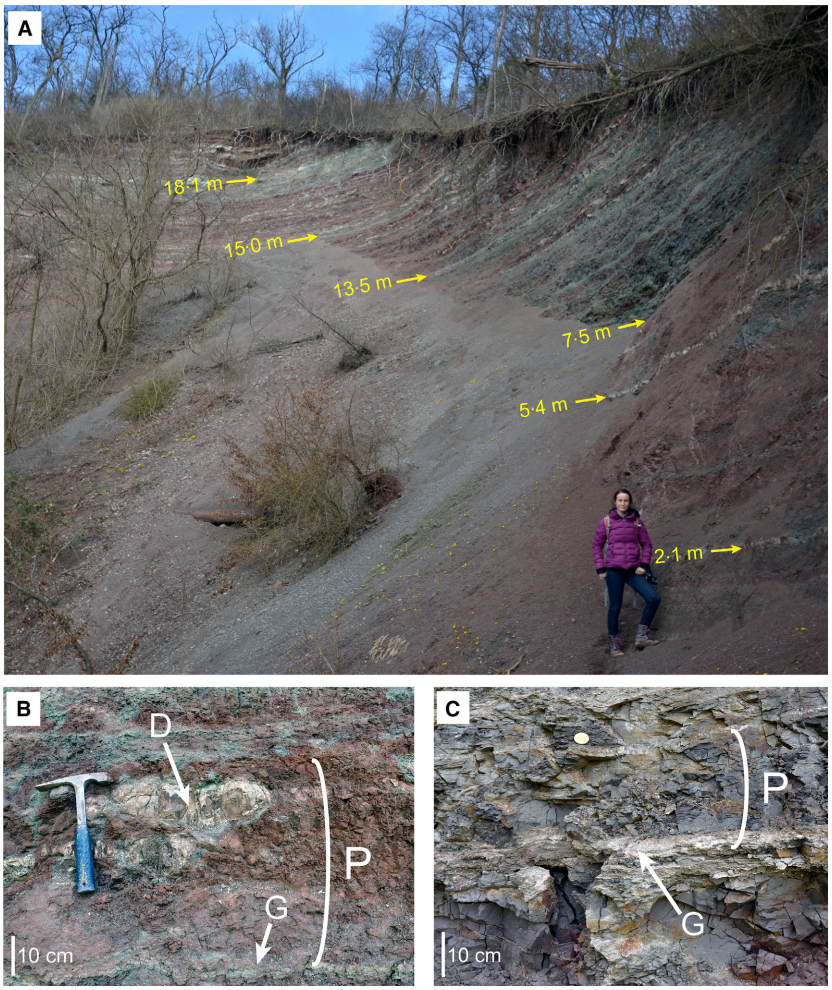

Fig. 4. (A) Image of the studied, 18·1 m high section of the Mainhardt Formation at Hohenhaslach (lowermost *ca* 1·9 m of the section are not visible). Person for scale is 1·68 m tall. Arrows denote distinct lithological features to facilitate direct comparison with Figs 5 and 8. (B) Lithological expression of a precession cycle from the 14·3 to 14·7 m interval, reflected by red–green couplets with intercalated gypsum beds and dolomite concretions. (C) Strata representing a precession cycle within the 8·0 to 8·5 m interval, dominated by greenish sediments with regularly spaced gypsum layers. D – dolomite, G – gypsum, P – lithological expression of a precession cycle.

5·40 m and 6·50 m (Fig. 5). From 7·50 to 12·15 m, alternating greenish grey to dark greenish grey, bluish grey and reddish claystones occur that are intercalated by greyish to reddish, 0·05 to 0·20 m thick irregular gypsum layers. Two up to 0·15 m thick dolomite beds are present at 11·70 m and 12·15 m.

The sediments that overlie the two dolomite beds up to the top of the section at 18·10 m consist of alternating red, oxidized, mottled and greenish grey claystones. Red, wavy gypsum layers become increasingly common towards the top of the section and often co-occur with increased silt contents in the surrounding mudstones. A prominent feature at 12·80 m is a *ca* 0·35 m thick breccia of monomictic claystone clasts. The breccia is succeeded by two *ca* 0·10 m thick dolomite beds at 13·35 m and 13·50 m. At *ca* 14·50 m, 16·20 m, 16·50 m and 16·90 m dolomite concretions with a diameter of up to 0·20 m are interbedded in reddish claystones, a feature not present at 14·50 m. A dolomite bed from 17·90 to 18·10 m forms the top of the section. The topmost dolomite bed is identified here as horizon sEII after Brenner (1973, 1978a,b) in accordance with earlier lithological descriptions of the Hohenhaslach outcrop by Brenner (1978a,b) and Reinhardt (2000).

Sediment colour

Sediment lightness (L^*) generally increases from the bottom to the top of the section with the notable presence of light–dark cycles with periods between 1 m and 2 m above *ca* 7·50 m section height (Fig. 5). The higher variability in sediment lightness above this horizon coincides with more distinct lithological alternations, although the metre-scale cyclicity in L^* is not reflected by analogous lithological features.

In the red–green ratio (a^*), a three-fold division of the section becomes apparent, parallel to the major lithological changes. The lower part of the section until *ca* 7·50 m exhibits a relatively low

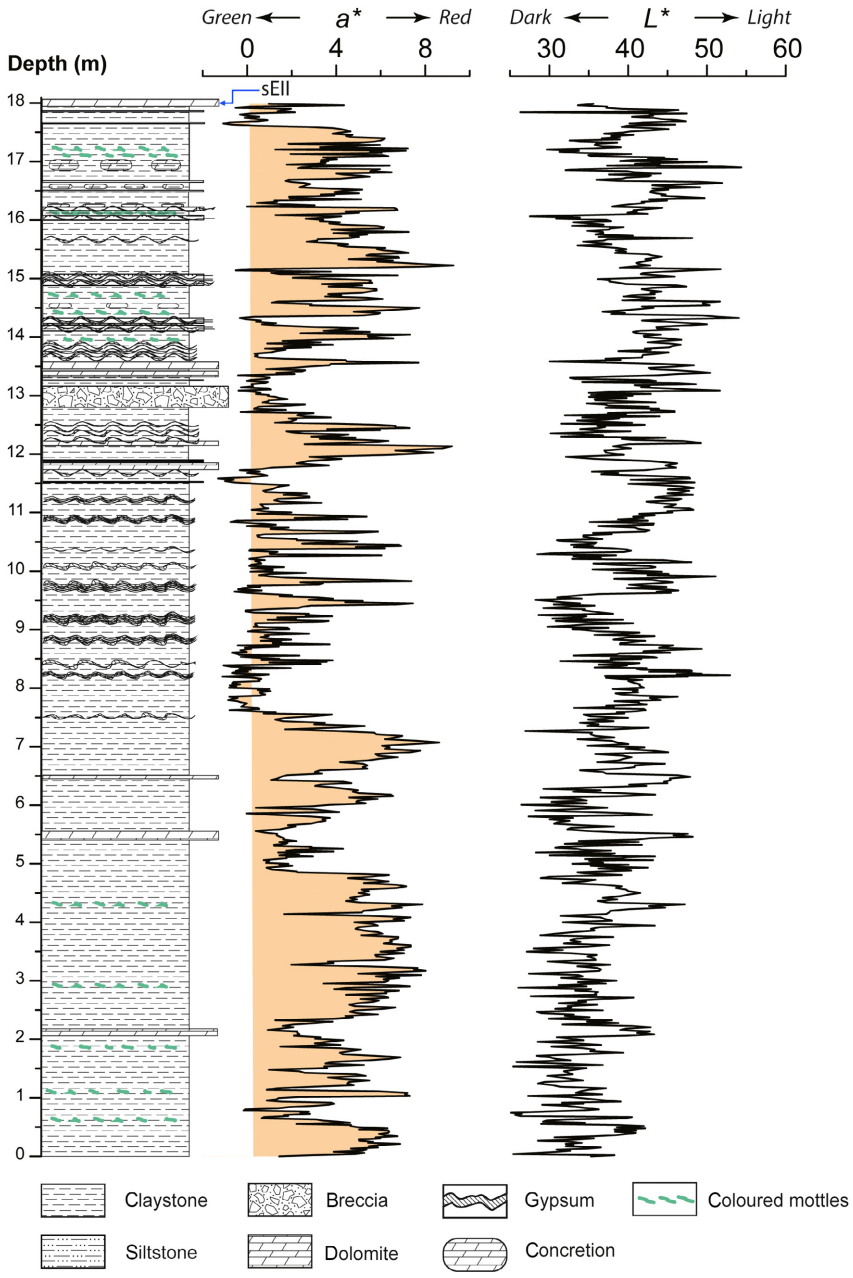

Fig. 5. Lithology of the Hohenhaslach section with colour values *a** (red–green ratio) and *L** (lightness). The distinct dolomite bank sEII after Brenner (1978a,b) and Reinhardt (2000) close to the top of the section is marked by a blue arrow.

*a** variability that reflects predominantly reddish colours (i.e. high *a**) with excursions to more greenish hues at 0·5 to 1·0 m, around 2·15 m and at 5·0 to 5·5 m. The middle part of the section, from *ca* 7·50 m to *ca* 12·15 m, displays a distinct, higher-frequency variability with a dominance of greyish and greenish (*a** close to zero) colours interrupted by regularly spaced, decimetre-scale spikes of higher *a** that correlate with the intercalated gypsum layers. The upper part of the section from *ca* 12·15 m onward is again dominated by high *a** (i.e. reddish colours), but with more internal variability than in the lowermost section. A distinct trend to low *a** is apparent between 12·0 m and 13·2 m, with the *a** minimum around 13·0 m coinciding with the distinct breccia at this depth.

DISCUSSION

Long-term evolution of the sedimentary system in the Hohenhaslach section

The facies changes and the colour variability documented in the Hohenhaslach section

suggest a three-phase evolution of the sedimentary system that was paced by distinct changes in the hydrological regime. During its first phase, which is represented by the lower part of the section until *ca* 7·50 m, the sedimentary sequence is dominated by hematite-rich, red claystones (Fig. 5). In accordance with the facies model developed for the Germanic Basin discussed above (Reinhardt, 2000; Reinhardt & Ricken, 2000; Vollmer, 2005; Vollmer *et al.*, 2008), these sediments can be associated with deposition during a phase of low playa-lake level under arid conditions. Subaerial exposure is documented by occasional greenish-grey mottling of the reddish claystones, which is caused by pedogenesis (Pimentel *et al.*, 1996; Tanner *et al.*, 2003). However, intercalated layers of greenish grey claystones point to more humid episodes that caused reducing pedogenic conditions; this is evident from the green colour of the sediment that reflects the prevalence of Fe^{2+} over Fe^{3+} (hydro-)oxides (i.e. low a^* values; Lyle, 1983; Kemp & Coe, 2007; Debret *et al.*, 2011; Fig. 5). Short-term expansions of the playa-lake during these episodes are further indicated by the formation of intercalated dolomite layers at 2·06 m, 5·40 m and 6·50 m. These dolomite layers occur within green-coloured intervals indicative of reducing conditions during high lake level. The dolomite beds show signs of polygonal cracking at their surfaces, derived from subaerial exposure, pointing to a marginal position within the playa-lake (Reinhardt & Ricken, 2000). Hence, the section until 7·50 m reflects predominantly arid conditions that were interrupted by transient humid episodes.

Between 7·50 m and 12·15 m, the depositional regime of the Hohenhaslach section was distinctly different, characterized by a dominance of greenish-grey claystones with rhythmically intercalated gypsum layers (Fig. 5). The change in sediment colour indicates predominately reducing depositional conditions associated with prolonged times of high playa-lake level (Lyle, 1983; Zhang *et al.*, 2007; Debret *et al.*, 2011). With regard to the long-term predominance of humid conditions, this phase resembles the earlier Carnian Pluvial Event of the mid-Carnian which has been associated with re-occurring phases of exceptionally strong monsoonal rainfall (Arche & López-Gómez, 2014; Ogg, 2015; López-Gómez *et al.*, 2017). The presence of decimetre-scale-thick interbedded gypsum layers suggests nonetheless short-term intervals of evaporation and regression of the playa-lake system. Finely dispersed hematite contributes to the red colour of the gypsum layers. Such alternations of mudstones and gypsum layers are typical for the playa successions of the Germanic Basin and represent the precession–driven fluctuation between wet and arid phases (Reinhardt & Ricken, 2000; Vollmer *et al.*, 2008).

The increasing dominance of reddish claystones associated with dolomite and gypsum precipitation from 12·50 to 18·10 m suggests the termination of the previous wetter climate phase and the return of mostly arid conditions; sedimentologically, this is documented by the development of a marginal playa/mudflat depositional system. The recurring succession of mudstone/gypsum/dolomite most likely represents precession cycles, as described from the Steinmergel–Keuper (Vollmer *et al.*, 2008). Here, gypsum saturation occurred after the monsoonal maximum (during minimal precession) when the playa-lake was nearly dried out, leading to gypsum co-precipitating with dolomite. Subsequent prolonged subaerial exposure during times of weak monsoon (high precession) is indicated by sediment mottling and dolocrete formation. However, even during times of a weak monsoon the groundwater table must have still been high enough to feed dolocrete formation by ascending pore waters due to capillary action (Rosen & Warren, 1990; Magee, 1991; Voigt *et al.*, 2017). The subordinate presence of greenish sediment colours indicates that high lake levels were rather short-lived episodes. Monomictic clay clasts between 12·8 m and 13·15 m constitute a peculiar part of this section; they might represent the remnant of a flash-flood event when clayey overbank deposits or the playa mudflat surface were eroded and transported as ripped-up mud clasts.

The facies evolution in the Hohenhaslach section as outlined above documents large-scale climate changes in the upper Carnian of the southern Germanic Basin. This finding agrees with recent evidence from both terrestrial and marine archives documenting that a transitional climate with relatively wet conditions persisted in the northern Tethyan realm and the Germanic Basin after the Carnian Pluvial Event (Hornung & Aigner, 2002; Roghi *et al.*, 2010; Stefani *et al.*, 2010; Arche & López-Gómez, 2014; McKie, 2014; López-Gómez *et al.*, 2017). Similarly humid conditions are documented for tropical Pangaea, such as on the Colorado Plateau (south-western

USA; Nordt *et al.*, 2015), in the Newark Basin (New Jersey, USA; Kent *et al.*, 2017), and in Southern China (Sun *et al.*, 2016), pointing to a relatively strong monsoonal precipitation in the low latitudes of Pangaea. In the following, this study further investigates the nature of the dry/wet phasing as observed in the Hohenhaslach section. A particular focus will be on constraining the influence of orbital forcing on sedimentation, which by extension will allow reconstruction of sedimentation rates for the Mainhardt Formation.

ORBITAL FORCING OF MEGA-MONSOON VARIABILITY DURING THE LATE CARNIAN

Previous studies of Triassic successions from the Germanic Basin (Steinmergelkeuper; Vollmer *et al.*, 2008), the Newark Basin (Olsen & Kent, 1996; Kent *et al.*, 2018; Olsen *et al.*, 2018, 2019), the Junggar Basin (North China; Sha *et al.*, 2015) and the Nanpanjiang Basin (South China; Fu *et al.*, 2016; Li *et al.*, 2016b) have provided strong evidence that their variability in sedimentary facies was paced by orbital precession, obliquity and eccentricity. In order to evaluate to what extent orbital forcing has also exerted influence on the late Carnian Gipskeuper deposits at Hohenhaslach, spectral analyses have been conducted on the obtained colour data.

Integrated over the entire Hohenhaslach section, the red–green (a^*) record shows significant periods (>95% confidence) of *ca* 3·30 m, *ca* 0·29 m, *ca* 0·21 m, *ca* 0·117 to 0·150 m and *ca* 0·102 m (Fig. 6). Spectral peaks of sediment lightness (L^*) are partially similar to those of a^*, with strong power between 0·104 to 0·137 m; in contrast they exhibit only weak power within the range of 0·20 to 0·30 m and long periods rather form a broad peak in the range of 1·15 to 2·80 m. In order to quantify the fit of the observed colour cycles to the orbital components, the Average Spectral Misfit (ASM) method was employed (Meyers & Sageman, 2007; Meyers *et al.*, 2012). Via a Monte Carlo simulation, this statistical method allows to test whether the null hypothesis of no orbital signal can be rejected for a given set of spectral peaks. The dominant cycles of the a^* power spectrum were employed here, because these have been used for cyclostratigraphic purposes in similar continental settings of Triassic age (Kemp & Coe, 2007; Vollmer *et al.*, 2008). In this regard, a^* is preferred over L^* because variations in sediment lightness are ambiguous in their relation to lithofacies, which renders them difficult to interpret with respect to palaeoenvironmental changes. The ASM spectrum was calculated such that it allowed sedimentation rates to range between 2 m and 100 m Myr^{-1} (Fig. 7). This assumption is based on sedimentation rates of 20 to 30 m Myr^{-1} as they have been inferred for the Norian Steinmergelkeuper Formation of the central Germanic Basin (i.e. the Morsleben section, Fig. 1; Vollmer *et al.*, 2008). The ASM results indicate that the best fit between spectral peaks and orbital target frequencies is given for a sedimentation rate between 7 m and 2 m Myr^{-1} [average sedimentation rate: 12 m Myr^{-1} reaching the critical significance level of H_0 (%) = 0·489]. This result shows that the null hypothesis H_o of no orbital forcing can be rejected (Fig. 7B).

In detail, the ASM results suggest that the observed *ca* 3·30 m a^* cycle relates to the *ca* 405 kyr period of eccentricity (E3), whereas the 0·29 m and 0·214 m cycles represent precession (21·4 kyr and 17·9 kyr for P1 and P2, respectively), and the 0·119 to 0·151 m cycles relate to half precession (HP). Because the astronomical configuration during the Triassic led to average orbital periods that differed from today, the orbital periods calculated for the Mesozoic by Laskar *et al.* (2004) were used. The assignment of the *ca* 3·30 m period to the E3 cycle is supported by the dominance of this period in the respective 3·30 m filter of both a^* and L^* with a notable anti-phasing (Fig. 8). This strong 3·30 m cycle is in line with previous findings, suggesting that E3 is the most stable and strongest Milankovitch cycle in climate records throughout Earth's history (Laskar *et al.*, 2004; Pälike *et al.*, 2006; Wang *et al.*, 2010; Olsen *et al.*, 2019). The persistence of the E3 cycle is due to the absence of any influence of tidal dissipation and the low impact of the chaotic orbital resonance, for example, in the Earth–Moon system (Lourens *et al.*, 2001). The dominance of the E3 cycle has also been shown for sedimentary records from the low-latitude (20 to 30°) records of the Newark and Germanic basins (Hambach *et al.*, 1999; Olsen & Kent, 1999; Reinhardt & Ricken, 1999, 2000; Reinhardt, 2000; Vollmer *et al.*, 2008) as well as from the high-latitude (60°) Junggar Basin (Northern China; Sha *et al.*, 2015). The lack of a clear short eccentricity (E1+2, *ca* 109 kyr) cycle in the a^* power-spectrum may be due to the ice-free greenhouse climate conditions of the late Triassic, which have been

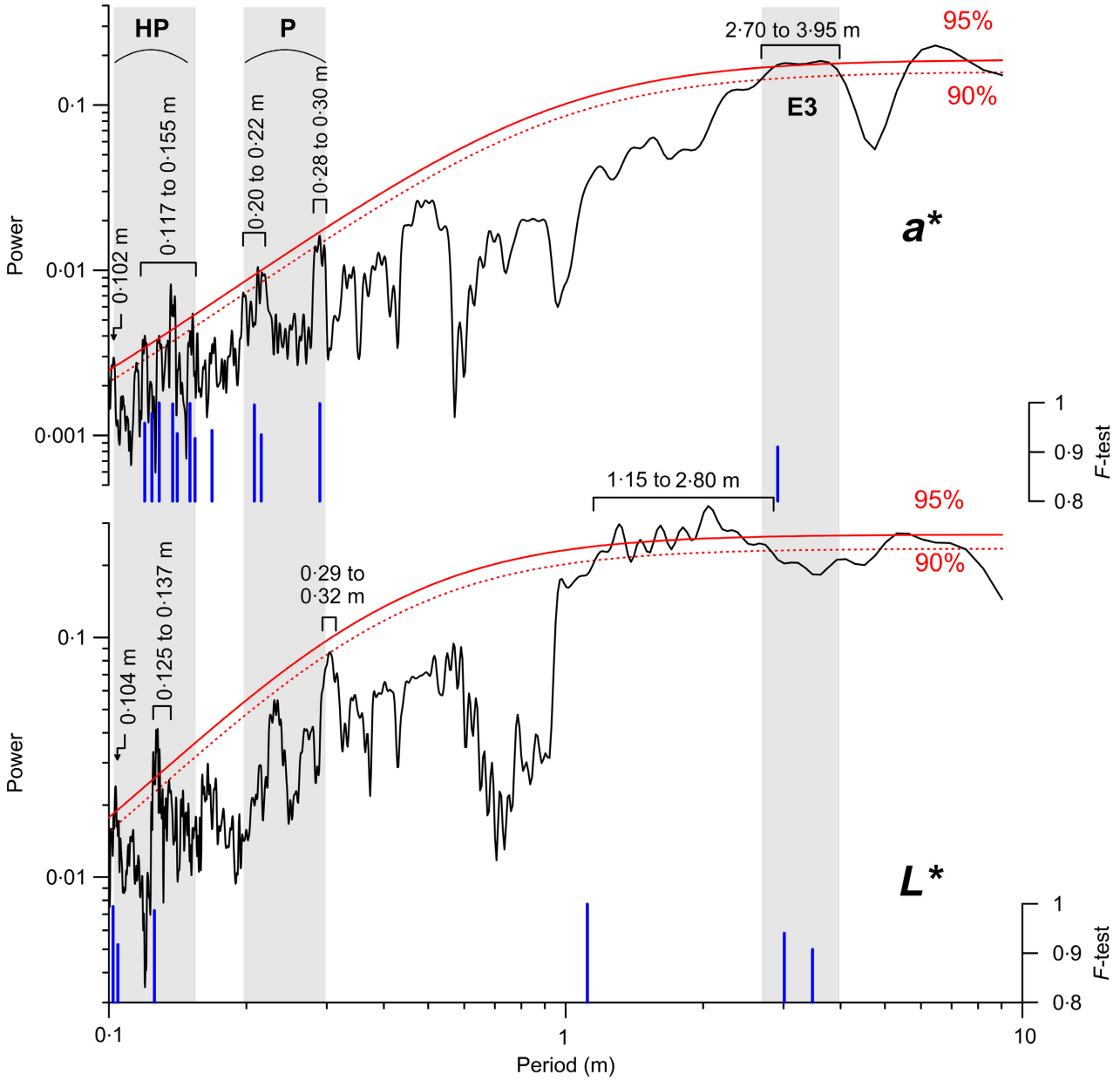

Fig. 6. Multitaper spectral analysis (with five tapers) of colour parameters *a** (red–green ratio) and *L** (lightness) of the Hohenhaslach section, with periods of *a** above the 95% significance level indicated by grey bars. Blue bars denote spectral peaks that are significant above the 90% level in an *F*-test. E, eccentricity; HP, half precession; P, precession.

argued to diminish the dominance of these cycles (Beaufort, 1994; Machlus *et al.*, 2008; Fu *et al.*, 2016). Considering the overall robustness of the *ca* 3·30 m cycle within the *a** and *L** records, and its association with the *ca* 405 kyr cycle, this study estimates the total time represented by the Hohenhaslach section to comprise six E3 cycles, which equals *ca* 2·4 Myr (Fig. 8). A duration of about *ca* 2·4 Myr for the Hohenhaslach section is within the limits of the yet relatively poorly constrained duration of the Mainhardt Formation (Heunisch & Nitsch, 2011; Franz *et al.*, 2018), and falls within the duration of the Tuvalian sub-stage, which comprises 5·1 Myr (Fig. 2; Kent *et al.*, 2017).

The influence of precession and eccentricity forcing may also explain the occurrence of the distinct humid phase between 7·50 m and 11·80 m in the Hohenhaslach section, which stands out against the long-term aridification

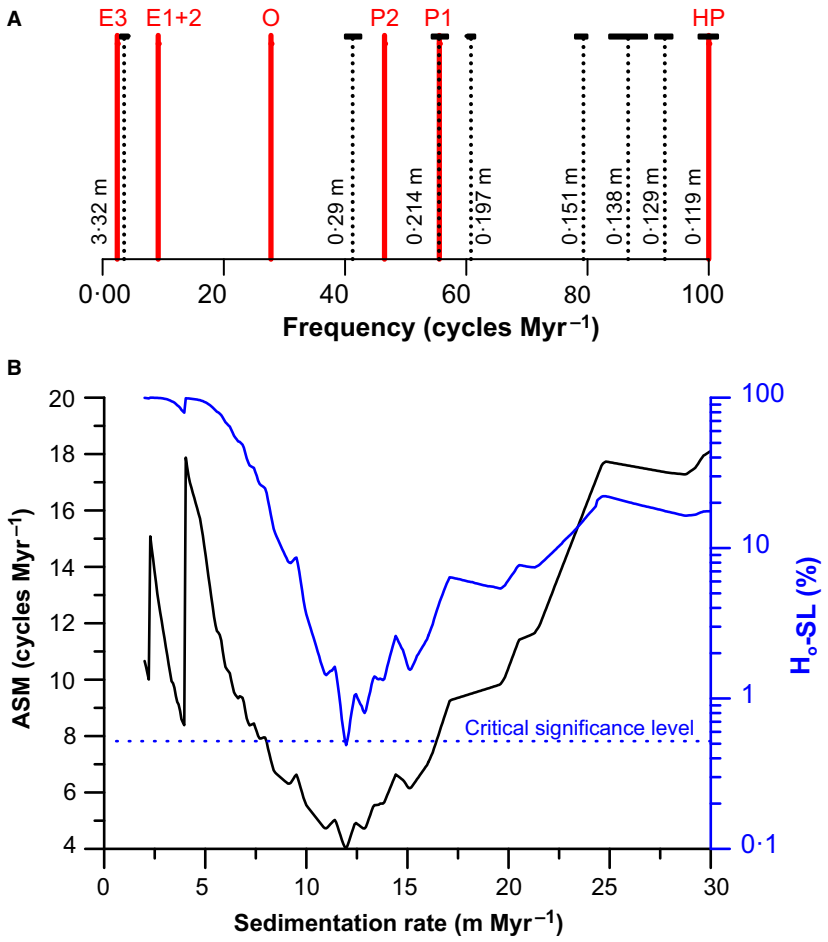

Fig. 7. Results of Average Spectral Misfit (ASM) calculations for frequencies with >95% confidence level in the *a** power-spectrum (Fig. 6) using 10^5 iterations for 400 sedimentation rates. (A) Relation of the spectral peaks (dashed black line; numbers indicate the respective periods in the depth domain) relative to the orbital target frequencies (red lines; E, eccentricity; HP, half precession; P, precession); black bars on top of spectral peaks denote the half-width of each peak; (B) ASM calculation (black line) and the significance level estimation for null hypothesis rejection (SL–H_o, blue line) with critical significance level indicated (dotted line). The results indicate that the null-hypothesis of no orbital forcing can be rejected (P = 0·0049), with the average sedimentation rate centred at 12 m Myr^{-1}. See text for further discussion.

across the Carnian–Norian boundary (Tanner, 2018). The *a** variability across this interval displays dominant periods of 0·20 m and 0·10 to 0·11 m (Figs 8 and 9). Filtering indicates that the 0·20 m periods are best captured by the red/green alternations (Fig. 10). These colour alternations suggest abrupt shifts between pronounced wet (predominance of greenish sediments) and dry phases (predominance of reddish sediments and gypsum precipitation) of the playa-lake system that are paced by precession. Furthermore, the amplitude of the *a** peaks is clearly modulated in this interval (Figs 8 and 10) as would be expected for a *ca* 405 kyr eccentricity maximum. Peak eccentricity causes a maximum in the amplitude of orbital precession and tropical summer insolation. As high summer insolation favours strong monsoonal rainfall, the intensification in precipitation might in turn have initiated this prolonged humid phase, as documented in the Hohenhaslach section. The often-observed bifurcation of the *a** peaks might be attributed to semi-precession cycles, which are a typical expression of the double insolation maximum in the low latitudes (Berger *et al.*, 2006; Verschuren *et al.*, 2009). The presence of a semi-precession beat in subtropical palaeolatitudes such as in Hohenhaslach is in line with previous findings from the Norian of the Germanic Basin (Vollmer *et al.*, 2008). The persistence of semi-precession signals across the basin therefore supports the propagation of low-latitude signals into higher latitudes via atmospheric teleconnections as inferred for Quaternary boundary conditions (Crowley *et al.*, 1992; Sun & Huang, 2006). In addition, the HP signal at Hohenhaslach might have been further amplified by the precipitation of dolomite and dolocrete layers when equinoxes were in perihelion and aphelion, respectively (see previous discussion of the facies model of Vollmer *et al.*, 2008), generating a carbonate double-peak during one precession cycle.

Although the ASM does not confirm the presence of an obliquity-related signal in the *a** record, the *ca* 1:10 ratio of the 0·29 to 0·22 m to

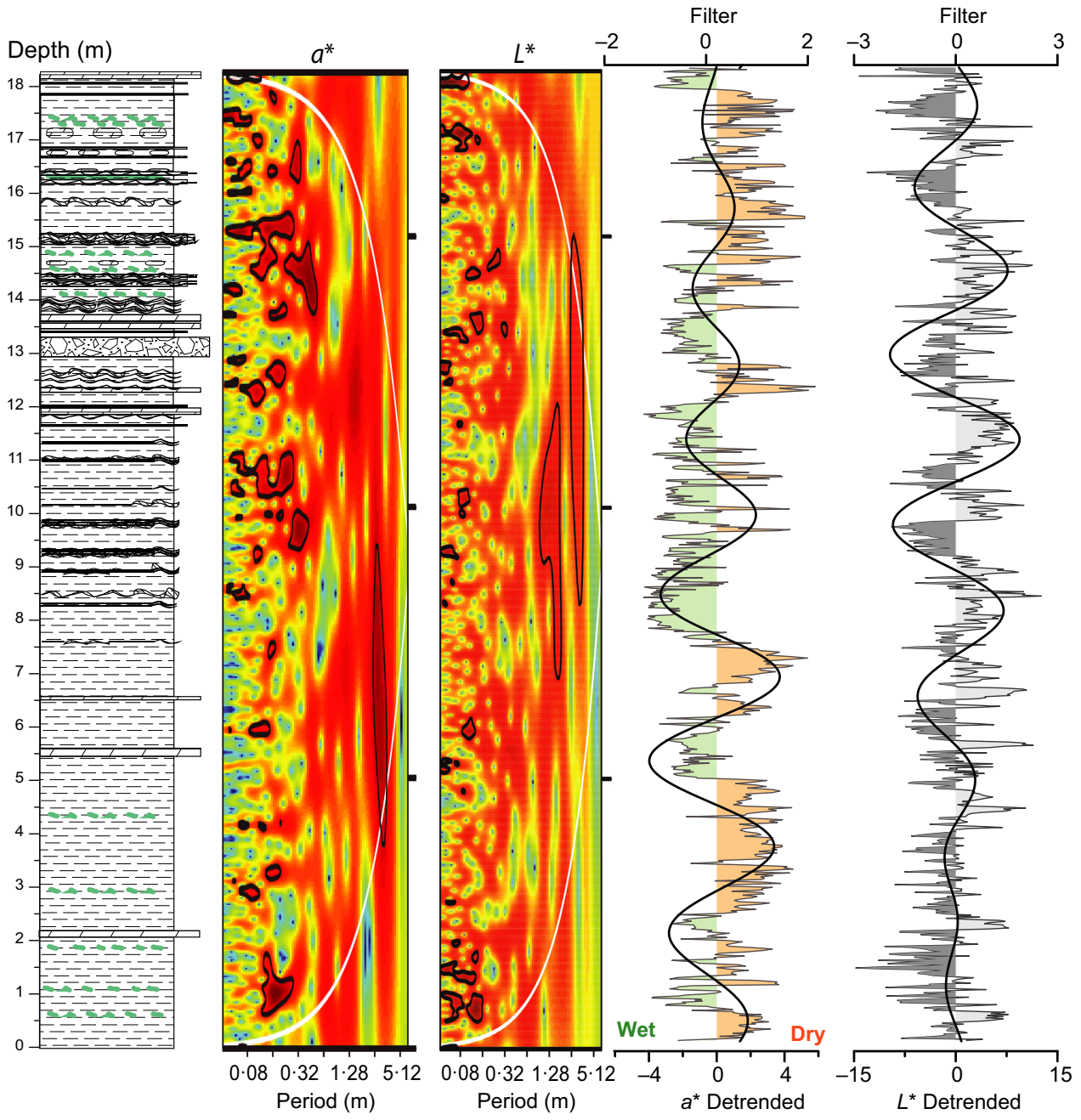

Fig. 8. Environmental variability of the Hohenhaslach section. The lithological evolution (legend cf. Fig. 5) is compared to the wavelets of colour parameters *a** and *L** (95% confidence levels are marked by black lines; the cone of influence in the wavelet plots are indicated by white lines) and the detrended colour data of *a** and *L** superimposed by a 3·30 m taner filter (bandwidth ± 0·60 m, roll-off rate = 10^5), presumed to represent the long *ca* 405 kyr eccentricity.

the *ca* 3·30 m cycles in *a** contradicts the *ca* 1:21 ratio between E3 and P1/P2. Therefore, 0·29 to 0·22 m cycles might instead be attributed to obliquity. However, the respective periods of the *a** signal are averaged over the entire section and might vary depending on the dominant deposition regime. Changes in sedimentation rate might also explain the discrepancy between the estimated total duration of *ca* 2·4 Myr for the deposition of the entire Hohenhaslach section based on the number of the E3 cycles (Fig. 8) and the actual average sedimentation rate of *ca* 12 m Myr^{-1}, which would rather imply the section to cover a time span of *ca* 1·8 Myr.

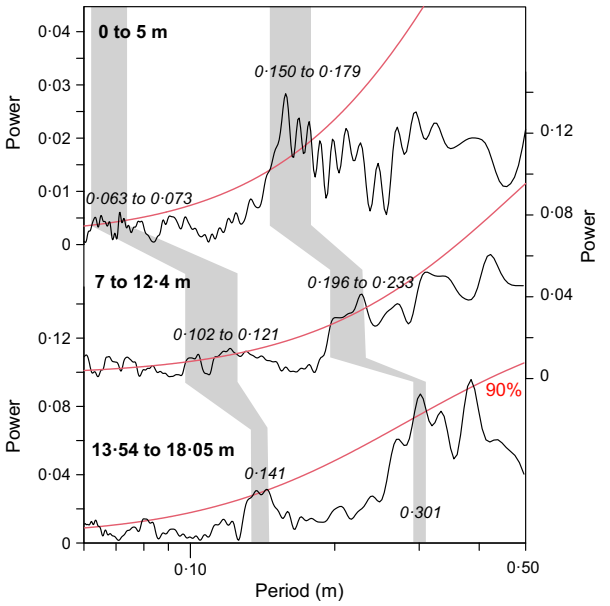

Fig. 9. Multitaper spectra (with three tapers) of colour parameter a^* (red–green ratio) for the three lithologically distinct sections of the Hohenhaslach section (depth intervals indicated next to the respective spectra) with 90% confidence intervals indicated. Grey bars indicate spectral peaks interpreted to represent precession (P) and half precession (HP). See text for further discussion.

To investigate the impact of changes in sedimentation rates on the a^* and L^* cycles, the spectral inventory of the three distinct depositional phases in the Hohenhaslach section were compared; these lithostratigraphic endmembers cover the intervals between 0·0 m and 5·0 m, 7·0 m and 12·4 m, and 13·5 m and 18·1 m. The individual spectral analyses of the respective sections in fact suggest changes in sedimentation rate (Fig. 9). Starting from the above assumption that the *ca* 0·20 m periods in the central unit represent precession and the 0·10 to 0·11 m periods semi-precession, the structure of the power-spectrum for the lowermost unit indicates equivalent periods of 0·325 m and 0·138 m, respectively. In contrast, the uppermost part of the section shows peaks at 0·145 to 0·18 m and 0·07 to 0·075 m, respectively. Based on these findings, the sedimentation rate declined from the bottom to the top of the section by a factor of about two, which caused the designated precession cycle to shift from a *ca* 0·32 m period in a^* (uppermost part of the section) to an average 0·16 m period (lowermost part of the section) (Fig. 9). Such a change in sedimentation rate can readily explain not only the offset between expected and reconstructed dominant frequencies, but also the relatively broad spectral peak at *ca* 3·30 m and the bundling of different highly significant peaks in the range of 0·10 to 0·15 m and 0·20 to 0·30 m for both a^* and L^* (Fig. 6).

The lack of a significant obliquity impact on the deposition of the strata preserved at Hohenhaslach is in line with evidence from other low-latitude settings, for example, the Newark Basin (USA) where a dominance of precession/eccentricity and a lack of clear obliquity modulation has been argued for (Sha *et al.*, 2015; Tanner & Lucas, 2015; Olsen *et al.*, 2019). At the same time, the present analysis contradicts the observation of an obliquity-related cyclicity in the Norian Steinmergelkeuper Formation of Morsleben (Vollmer, 2005; Vollmer *et al.*, 2008) from the central Germanic Basin (Fig. 1). This mismatch could be explained by the northward shift of the Germanic Basin into higher palaeolatitudes by *ca* 15° during the Norian (Kent & Tauxe, 2005; Kent *et al.*, 2014). In addition, Vollmer *et al.* (2008) argued that their obliquity signal relates to dust input originating from the higher latitudes of Northern China. The increasingly drier and hotter climate during the Norian might have led to more geographically extensive deserts and subsequently to a stronger direct dust flux southward into the low latitudes (Talbot *et al.*, 1994).

The consistency of the facies successions and the relations of dominant frequencies in the colour spectrum to orbital parameters, as documented in the data here, strongly support an external, climatic control on the depositional system exposed in the Hohenhaslach section. The statistically robust presence of Milankovitch-related periodicities similar to those found in other late Triassic sections from across the Germanic Basin (Reinhardt, 2000; Vollmer, 2005; Vollmer *et al.*, 2008) further argues in favour of semi-continuous deposition interrupted by only minor hiatuses (Franz *et al.*, 2018). The presence of marker horizon 'sEII' (Brenner, 1973, 1978a; Reinhardt, 2000), which can be correlated across the southern Germanic Basin for more than 125 km (Brenner, 1978a,b, 1979; Reinhardt, 2000), also indicates that the studied sediment succession reflects regional-scale palaeoenvironmental changes. Hence, the authors consider autocyclical processes (Tanner, 2010) and regional tectonics (Hornung & Brandner, 2005; Kozur & Bachmann, 2010; Arche & López-Gómez, 2014) to be of

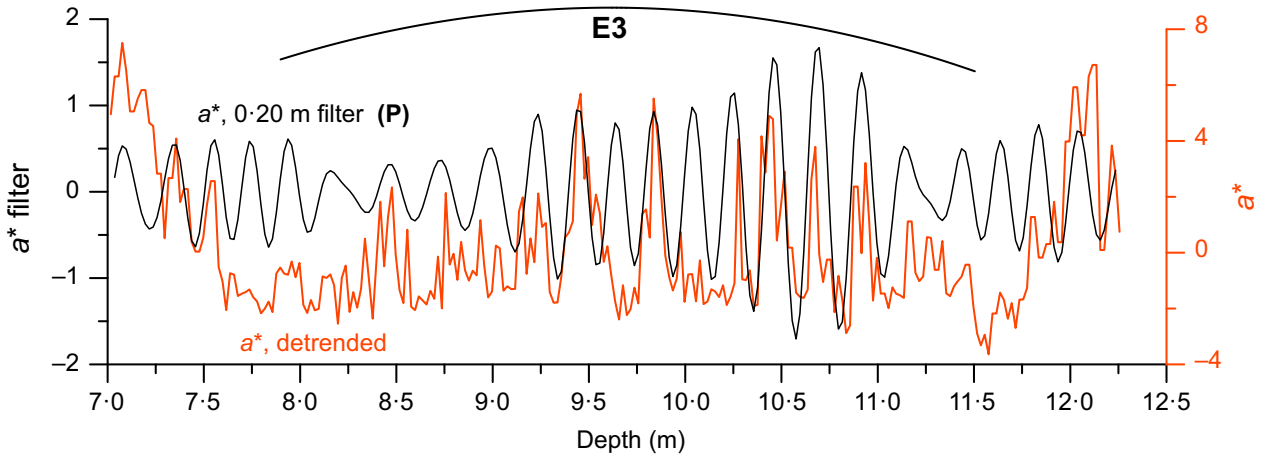

Fig. 10. Detrended red–green ratio (a^*, orange line) for the interval 7·00 to 12·40 m of the Hohenhaslach section. This interval displays the most distinct alternations between green and red claystones with regularly interbedded gypsum layers (cf. Fig. 5). The colour and lithology changes are interpreted to reflect the alternation between humid and arid phases giving rise to green and red sediment colours, respectively. The red–green variations are dominated by a cyclicity of *ca* 0·20 m (Fig. 9), as supported by a taner bandpass filter of a^* (black line) centred at 0·20 m with a bandwidth of ±0·053 m and a roll-off rate of 10^5. The *ca* 0·20 m period presumably represents precession (P), modulated by the E3 eccentricity cycle. See text for further discussion.

subordinate importance for the development of the playa and alluvial fan system at Hohenhaslach.

These findings also strongly advocate that orbital pacing, in particular long eccentricity, may have played a so far underestimated role for pacing humid climate pulses during the Triassic. The progressive uplift of the Fennoscandian Massif may have played an important role in this respect because it reached heights in excess of *ca* 2000 m during the mid-Carnian (Arche & López-Gómez, 2014), an elevation considered as the orographic rainfall threshold based on the Cenozoic uplift of the Himalayan mountains (Ding *et al.*, 2017). The uplift of the Fennoscandian Massif might have caused increased rainfall over the Germanic Basin during the Carnian via orographic blocking and initiated widespread changes in atmospheric circulation pattern that enhanced seasonal precipitation in the (sub)tropics (Arche & López-Gómez, 2014). An intensification of the wet season naturally increased the seasonality of the annual precipitation cycle. The authors speculate that an enhanced seasonality would have increased the sensitivity of the Pangaean monsoonal system to orbital precession and eccentricity via their control on the seasonal low-latitude insolation cycle. The progressive weakening of wet phases during the Norian could then be attributed to the subsequent erosion of the Fennoscandian Massif.

CONCLUSIONS

Playa and alluvial fan sediments from the Mainhardt Formation of the Tuvalian (latest Carnian) in the south-western Germanic Basin provide new insight into the palaeoenvironmental evolution during the late Triassic against the background of the 'mega-monsoon' system prevailing at that time. This study found distinct, statistically highly significant cyclicities in the red–green (a^*) and lightness (L^*) spectra that reflect recurring sediment-facies patterns. Arid phases are dominated by distal alluvial fan fines and reddish sediment colours (high a^*), while more humid phases are reflected by a higher playa-lake level, increased pedogenesis and greenish colours (low a^*). The internal relation of dominant spectral peaks in the a^* record allows identification of precession and long (*ca* 405 kyr) eccentricity-related periods. The dominance of the precession signal testifies to the dominant low-latitude forcing of the monsoonal system during this time period. In turn, the monsoonal system modulated moisture content and thus playa-lake level and groundwater table.

A distinct obliquity signal could not be identified in these sedimentary records in contrast to the Norian Steinmergelkeuper Formation of the Germanic Basin. It is likely that the documented long-term drought from the late Carnian to the Norian and the northward drift of the Germanic Basin played a profound role for the low-latitude

propagation of the obliquity signal because dust flux has been proposed as a major contributor to the obliquity impact in the Steinmergelkeuper.

This study also found a prolonged phase of high playa-lake level related to a *ca* 405 kyr-eccentricity maximum that fostered exceptionally strong monsoonal rainfall. This period bears resemblance to conditions proposed to have occurred during the Carnian Pluvial Event, indicating the persistence of humid pulses during the latest Carnian.

ACKNOWLEDGEMENTS

D. and U. Hofstädter provided generous logistical support during fieldwork. R.-E. Waldhör is thanked for on-site discussions. GK acknowledges financial support for fieldwork by Heidelberg University. N. Preto and six anonymous referees are thanked for thoughtful, constructive reviews. Open access funding enabled and organized by Projekt DEAL.

DATA AVAILABILITY STATEMENT

The spectrophotometric data is available in the Appendix S1 accompanying this manuscript.

REFERENCES

Aigner, T. and **Bachmann, G.H.** (1989) Dynamic stratigraphy of an evaporite-to-red bed sequence, Gipskeuper (Triassic), southwest German Basin. *Sed. Geol.*, **62**, 5–25.

Aigner, T. and **Bachmann, G.H.** (1992) Sequence-stratigraphic framework of the German Triassic. *Sed. Geol.*, **80**, 115–135.

Arche, A. and **López-Gómez, J.** (2014) The Carnian Pluvial Event in Western Europe: new data from Iberia and correlation with the Western Neotethys and Eastern North America–NW Africa regions. *Earth Sci. Rev.*, **128**, 196–231.

Bachmann, G.H. and **Kozur, H.W.** (2015) The Germanic Triassic: correlations with the international chronostratigraphic scale, numerical ages and Milankovitch cyclicity. *Hallesches Jahrbuch für Geowissenschaften*, **26**, 17–62.

Beaufort, L. (1994) Climatic importance of the modulation of the 100 kyr cycle inferred from 16 m.y. long Miocene records. *Paleoceanography*, **9**, 821–834.

Berger, A., **Loutre, M.F.** and **Mélice, J.L.** (2006) Equatorial insolation: from precession harmonics to eccentricity frequencies. *Clim. Past*, **2**, 131–136.

Bernardi, M., **Gianolla, P.**, **Petti, F.M.**, **Mietto, P.** and **Benton, M.J.** (2018) Dinosaur diversification linked with the Carnian Pluvial Episode. *Nat. Commun.*, **9**, 1499.

Berra, F., **Jadoul, F.** and **Anelli, A.** (2010) Environmental control on the end of the Dolomia Principale/Hauptdolomit depositional system in the central Alps: coupling sea-level and climate changes. *Palaeogeogr. Palaeoclimatol. Palaeoecol.*, **290**, 138–150.

Boigk, H., **Schöneich, H.**, **Illies, J.** and **Fuchs, K.** (1974) Perm, Trias und älterer Jura im Bereich der südlichen Mittelmeer-Mjösen-Zone und des Rheingrabens. *Proc. Int. Rift Symposium*, **8**, 60–71.

Bosmans, J., **Drijfhout, S.**, **Tuenter, E.**, **Hilgen, F.** and **Lourens, L.** (2015a) Response of the North African summer monsoon to precession and obliquity forcings in the EC-Earth GCM. *Clim. Dyn.*, **44**, 279–297.

Bosmans, J., **Drijfhout, S.**, **Tuenter, E.**, **Hilgen, F.**, **Lourens, L.** and **Rohling, E.** (2015b) Precession and obliquity forcing of the freshwater budget over the Mediterranean. *Quatern. Sci. Rev.*, **123**, 16–30.

Bragin, N.Y., **Konstantinov, A.** and **Sobolev, E.** (2012) Upper Triassic stratigraphy and paleobiogeography of Kotel'nyi Island (New Siberian Islands). *Stratigr. Geol. Correl.*, **20**, 541–566.

Brenner, K. (1973) Stratigraphie und Paläogeographie des Oberen Mittelkeupers in Südwest-Deutschland. *Arbeiten aus dem Institut für Geologie und Paläontologie der Universität Stuttgart*, **68**, 101–222.

Brenner, K. (1978a) Profile aus dem Oberen Mittelkeuper Südwest-Deutschlands. *Arbeiten aus dem Institut für Geologie und Paläontologie der Universität Stuttgart*, **72**, 103–203.

Brenner, K. (1978b) Sammlung und Revision der bis 1978 veröffentlichten Profile aus dem Oberen Mittelkeuper Südwest-Deutschlands. *Arbeiten aus dem Institut für Geologie und Paläontologie der Universität Stuttgart*, **72**, 205–239.

Brenner, K. (1979) Paläogeographische Raumbilder Südwestdeutschlands für die Ablagerungszeit von Kiesel- und Stubensandstein. *Jahresberichte und Mitteilungen des Oberrheinischen Geologischen Vereins*, **61**, 331–335.

Carlé, W. and **Linck, O.** (1949) Die Strombergmulde im nordwestlichen Württemberg. *Jahrbuch für Mineralogie, Geologie und Paläontologie, Abhandlungen*, **90**, 427–478.

Crowley, T.J., **Kim, K.-Y.**, **Mengel, J.G.** and **Short, D.A.** (1992) Modeling 100,000-year climate fluctuations in pre-Pleistocene time series. *Science*, **255**, 705–707.

Dal Corso, J., **Gianolla, P.**, **Rigo, M.**, **Franceschi, M.**, **Roghi, G.**, **Mietto, P.**, **Manfrin, S.**, **Raucsik, B.**, **Budai, T.**, **Jenkyns, H.C.**, **Reymond, C.E.**, **Caggiati, M.**, **Gattolin, G.**, **Breda, A.**, **Merico, A.** and **Preto, N.** (2018) Multiple negative carbon-isotope excursions during the Carnian Pluvial Episode (Late Triassic). *Earth Sci. Rev.*, **185**, 732–750.

Debret, M., **Sebag, D.**, **Desmet, M.**, **Balsam, W.**, **Copard, Y.**, **Mourier, B.**, **Susperrigui, A.S.**, **Arnaud, F.**, **Bentaleb, I.**, **Chapron, E.**, **Lallier-Vergès, E.** and **Winiarski, T.** (2011) Spectrocolorimetric interpretation of sedimentary dynamics: The new "Q7/4 diagram". *Earth Sci. Rev.*, **109**, 1–19.

Ding, L., **Spicer, R.**, **Yang, J.**, **Xu, Q.**, **Cai, F.**, **Li, S.**, **Lai, Q.**, **Wang, H.**, **Spicer, T.** and **Yue, Y.** (2017) Quantifying the rise of the Himalaya orogen and implications for the South Asian monsoon. *Geology*, **45**, 215–218.

Dubiel, R.F., **Parrish, J.T.**, **Parrish, J.M.** and **Good, S.C.** (1991) The Pangaean megamonsoon: evidence from the Upper Triassic Chinle Formation, Colorado Plateau. *Palaios*, 347–370.

Fischer, J., **Voigt, S.**, **Franz, M.**, **Schneider, J.W.**, **Joachimski, M.M.**, **Tichomirowa, M.**, **Götze, J.** and **Furrer, H.** (2012) Palaeoenvironments of the late Triassic Rhaetian Sea: Implications from oxygen and strontium isotopes of

hybodont shark teeth. *Palaeogeogr. Palaeoclimatol. Palaeoecol.*, **353–355**, 60–72.

Franz, M., **Bachmann, G.H.**, **Barnasch, J.**, **Heunisch, C.** and **Röhling, H.-G.** (2018) The Keuper Group in the Stratigraphic Table of Germany 2016 – continuous sedimentation in the North German Basin (variant B). *Z. Dt. Ges. Geowiss.*, **169**, 203–224.

Fu, W., **Jiang, D.-Y.**, **Montañez, I.P.**, **Meyers, S.R.**, **Motani, R.** and **Tintori, A.** (2016) Eccentricity and obliquity paced carbon cycling in the Early Triassic and implications for post-extinction ecosystem recovery. *Sci. Rep.*, **6**, 27793.

Furin, S., **Preto, N.**, **Rigo, M.**, **Roghi, G.**, **Gianolla, P.**, **Crowley, J.L.** and **Bowring, S.A.** (2006) High-precision U-Pb zircon age from the Triassic of Italy: Implications for the Triassic time scale and the Carnian origin of calcareous nannoplankton and dinosaurs. *Geology*, **34**, 1009–1012.

Gastaldo, R.A., **Neveling, J.**, **Geissman, J.W.** and **Li, J.** (2019) A multidisciplinary approach to review the vertical and lateral facies relationships of the purported vertebrate-defined terrestrial Permian-Triassic boundary interval at Bethulie, Karoo Basin, South Africa. *Earth Sci. Rev.*, **189**, 220–243.

Geluk, M.C. and **Röhling, H.-G.** (1997) High-resolution sequence stratigraphy of the Lower Triassic 'Buntsandstein' in the Netherlands and northwestern Germany. *Geol. Mijnbouw*, **76**, 227–246.

Geyer, O.F., **Gwinner, M.P.**, **Geyer, M.**, **Nitsch, E.** and **Simon, T.** (2011) *Geologie von Baden-Württemberg*. Schweizerbart, Stuttgart, 627 pp.

Götz, A.E. (2002) Hochauflösende Stratigraphie im Unteren Muschelkalk (Mitteltrias, Anis) des Germanischen Beckens. *Schriftenr. Deutsch. Geol. Ges*, **15**, 101–107.

Götz, A. and **Wertel, C.** (2002) Zyklische Sedimentation im Unteren Muschelkalk. *Schriftenr. Deutsch. Geol. Ges*, **18**, 37–44.

Gouhier, T.C., **Grinsted, A.** and **Simko, V.** (2016). R package 'biwavelet'. Available at: https://github.com/tgouhier/biwavelet.

Gradstein, F.M., **Ogg, J.G.**, **Schmitz, M.** and **Ogg, G.** (2012) *The geologic time scale 2012*. Elsevier, Boston, USA.

Hambach, U., **Reinhardt, L.**, **Wonik, T.**, **Port, G.**, **Krumsiek, K.** and **Ricken, W.** (1999) Orbital forcing in a low-latitude playa system: evidence from evolutionary spectral analyses (ESA) of geophysical and geochemical data from the Steinmergel-Keuper (Late Triassic, S-Germany). *Terra Nostra*, **99**, 97–100.

Heunisch, C. and **Nitsch, E.** (2011) Eine seltene Mikroflora aus der Mainhardt-Formation (Keuper, Trias) von Baden-Württemberg (Süddeutschland). *Jahresberichte und Mitteilungen des Oberrheinischen Geologischen Vereins*, **93**, 55–76.

Hornung, J. and **Aigner, T.** (2002) Reservoir architecture in a terminal alluvial plain: an outcrop analogue study (Upper Triassic, Southern Germany) Part II: cyclicity, controls and models. *J. Pet. Geol*, **25**, 151–178.

Hornung, T. and **Brandner, R.** (2005) Biochronostratigraphy of the Reingraben Turnover (Hallstatt Facies Belt): Local black shale events controlled by regional tectonics, climatic change and plate tectonics. *Facies*, **51**, 460–479.

Hornung, T., **Krystyn, L.** and **Brandner, R.** (2007) A Tethys-wide mid-Carnian (Upper Triassic) carbonate productivity crisis: Evidence for the Alpine Reingraben Event from Spiti (Indian Himalaya)? *J. Asian Earth Sci.*, **30**, 285–302.

Kedzierski, J. (2000) Sequenzstratigraphie des Muschelkalks im östlichen Teil des Germanischen Beckens. Diss. Univ. Halle.

Kemp, D.B. and **Coe, A.L.** (2007) A nonmarine record of eccentricity forcing through the Upper Triassic of southwest England and its correlation with the Newark Basin astronomically calibrated geomagnetic polarity time scale from North America. *Geology*, **35**, 991–994.

Kent, D.V. and **Olsen, P.E.** (2000) Magnetic polarity stratigraphy and paleolatitude of the Triassic-Jurassic Blomidon Formation in the Fundy basin (Canada): implications for early Mesozoic tropical climate gradients. *Earth Planet. Sci. Lett.*, **179**, 311–324.

Kent, D.V. and **Tauxe, L.** (2005) Corrected Late Triassic latitudes for continents adjacent to the North Atlantic. *Science*, **307**, 240–244.

Kent, D.V., **Malnis, P.S.**, **Colombi, C.E.**, **Alcober, O.A.** and **Martínez, R.N.** (2014) Age constraints on the dispersal of dinosaurs in the Late Triassic from magnetochronology of the Los Colorados Formation (Argentina). *Proc. Natl Acad. Sci. USA*, **111**, 7958–7963.

Kent, D.V., **Olsen, P.E.** and **Muttoni, G.** (2017) Astrochronostratigraphic polarity time scale (APTS) for the Late Triassic and Early Jurassic from continental sediments and correlation with standard marine stages. *Earth Sci. Rev.*, **166**, 153–180.

Kent, D.V., **Olsen, P.E.**, **Rasmussen, C.**, **Lepre, C.**, **Mundil, R.**, **Irmis, R.B.**, **Gehrels, G.E.**, **Giesler, D.**, **Geissman, J.W.** and **Parker, W.G.** (2018) Empirical evidence for stability of the 405-kiloyear Jupiter-Venus eccentricity cycle over hundreds of millions of years. *Proc. Natl Acad. Sci. USA*, **115**, 6153–6158.

Kidder, D.L. and **Worsley, T.R.** (2004) Causes and consequences of extreme Permo-Triassic warming to globally equable climate and relation to the Permo-Triassic extinction and recovery. *Palaeogeogr. Palaeoclimatol. Palaeoecol.*, **203**, 207–237.

Kirby, C., **Decker, S.** and **Macander, N.** (1999) Comparison of color, chemical and mineralogical compositions of mine drainage sediments to pigment. *Environ. Geol.*, **37**, 243–254.

Kozur, H.W. and **Bachmann, G.H.** (2005) Correlation of the Germanic Triassic with the international scale. *Albertiana*, **32**, 21–35.

Kozur, H.W. and **Bachmann, G.** (2010) The Middle Carnian wet intermezzo of the Stuttgart formation (Schilfsandstein), Germanic Basin. *Palaeogeogr. Palaeoclimatol. Palaeoecol.*, **290**, 107–119.

Kutzbach, J.E. (1994) Idealized Pangean climates: sensitivity to orbital change. *Geol. Soc. Am. Spec. Paper*, **288**, 41–56.

Kutzbach, J. and **Gallimore, R.** (1989) Pangaean climates: megamonsoons of the megacontinent. *J. Geophys. Res. Atmos.*, **94**, 3341–3357.

Kutzbach, J.E. and **Liu, Z.** (1997) Response of the African Monsoon to orbital forcing and ocean feedbacks in the Middle Holocene. *Science*, **278**, 440–443.

Laskar, J., **Robutel, P.**, **Joutel, F.**, **Gastineau, M.**, **Correia, A.C.M.** and **Levrard, B.** (2004) A long-term numerical solution for the insolation quantities of the Earth. *Astron. Astrophys.*, **428**, 261–285.

Lee, J.-Y. and **Wang, B.** (2014) Future change of global monsoon in the CMIP5. *Clim. Dyn.*, **42**, 101–119.

LGRB (Landesamt für Geologie, Rohstoffe und Bergbau) (2000) Blatt 6920 Brackenheim. In: *Geologische Karte von Baden-Württemberg 1:25000* (Ed. I. Kleingoor). LGRB, Freiburg im Breisgau, 29 pp.

LGRB (Landesamt für Geologie, Rohstoffe und Bergbau) (2001) Blatt 6919 Güglingen, vorläufige Ausgabe. In: *Geologische Karte von Baden-Württemberg 1:25000* (Ed. I. Kleingoor). LGRB, Freiburg im Breisgau, 15 pp.

LGRB (Landesamt für Geologie, Rohstoffe und Bergbau) (2016) *Symbolschlüssel Geologie Baden-Württemberg – Verzeichnis Geologischer Einheiten (aktualisierte Ausgabe 2016)*. Landesamt für Geologie, Rohstoffe und Bergbau, Regierungspräsidium Freiburg, 51 pp.

Li, M., **Huang, C.**, **Hinnov, L.**, **Ogg, J.**, **Chen, Z.-Q.** and **Zhang, Y.** (2016a) Obliquity-forced climate during the Early Triassic hothouse in China. *Geology*, **44**, 623–626.

Li, M., **Ogg, J.**, **Zhang, Y.**, **Huang, C.**, **Hinnov, L.**, **Chen, Z.-Q.** and **Zou, Z.** (2016b) Astronomical tuning of the end-Permian extinction and the Early Triassic Epoch of South China and Germany. *Earth Planet. Sci. Lett.*, **441**, 10–25.

López-Gómez, J., **Escudero-Mozo, M.**, **Martín-Chivelet, J.**, **Arche, A.**, **Lago, M.** and **Galé, C.** (2017) Western Tethys continental-marine responses to the Carnian Humid Episode: Palaeoclimatic and palaeogeographic implications. *Global Planet. Change*, **148**, 79–95.

Lourens, L.J., **Antonarakou, A.**, **Hilgen, F.**, **Van Hoof, A.**, **Vergnaud-Grazzini, C.** and **Zachariasse, W.** (1996) Evaluation of the Plio-Pleistocene astronomical timescale. *Paleoceanogr. Paleoclimatol.*, **11**, 391–413.

Lourens, L.J., **Wehausen, R.** and **Brumsack, H.J.** (2001) Geological constraints on tidal dissipation and dynamical ellipticity of the Earth over the past three million years. *Nature*, **409**, 1029–1033.

Lyle, M. (1983) The brown-green color transition in marine sediments: A marker of the Fe (III)-Fe (II) redox boundary. *Limnol. Oceanogr.*, **28**, 1026–1033.

Machlus, M.L., **Olsen, P.E.**, **Christie-Blick, N.** and **Hemming, S.R.** (2008) Spectral analysis of the lower Eocene Wilkins Peak Member, Green River Formation, Wyoming: Support for Milankovitch cyclicity. *Earth Planet. Sci. Lett.*, **268**, 64–75.

Magee, J. (1991) Late Quaternary lacustrine, groundwater, aeolian and pedogenic gypsum in the Prungle Lakes, southeastern Australia. *Palaeogeogr. Palaeoclimatol. Palaeoecol.*, **84**, 3–42.

Mazza, M., **Furin, S.**, **Spötl, C.** and **Rigo, M.** (2010) Generic turnovers of Carnian/Norian conodonts: Climatic control or competition? *Palaeogeogr. Palaeoclimatol. Palaeoecol.*, **290**, 120–137.

McKie, T. (2014) Climatic and tectonic controls on Triassic dryland terminal fluvial system architecture, central North Sea. *Int. Assoc. Sedimentol. Spec. Publ.*, **42**, 19–57.

Mertz, K.A. and **Hubert, J.F.** (1990) Cycles of sand-flat sandstone and playa–lacustrine mudstone in theTriassic–Jurassic Blomidon redbeds, Fundy rift basin, Nova Scotia: implications for tectonic and climatic controls. *Can. J. Earth Sci.*, **27**, 442–451.

Meyers, S. (2014) Astrochron: An R package for astrochronology. Available at http: org/web/packages/astrochron/index.html

Meyers, S.R. and **Sageman, B.B.** (2007) Quantification of deep-time orbital forcing by average spectral misfit. *Am. J. Sci.*, **307**, 773–792.

Meyers, S.R., **Sageman, B.B.** and **Arthur, M.A.** (2012) Obliquity forcing of organic matter accumulation during Oceanic Anoxic Event 2. *Paleoceanography*, **27**, PA3212.

Miller, C.S., **Peterse, F.**, **Da Silva, A.-C.**, **Baranyi, V.**, **Reichart, G.J.** and **Kürschner, W.M.** (2017) Astronomical age constraints and extinction mechanisms of the Late Triassic Carnian crisis. *Sci. Rep.*, **7**, 2557.

Mohtadi, M., **Prange, M.** and **Steinke, S.** (2016) Palaeoclimatic insights into forcing and response of monsoon rainfall. *Nature*, **533**, 191–199.

Mutti, M. and **Weissert, H.** (1995) Triassic monsoonal climate and its signature in Ladinian-Carnian carbonate platforms (Southern Alps, Italy). *J. Sediment. Res.*, **65**, 357–367.

Nairn, A. and **Smithwick, M.** (1976) Permian paleogeography and climatology. *The Continental Permian in Central, West, and South Europe: Boston, D. Reidel*, 283–312.

Nitsch, E. (2018) Der Keuper in der Stratigraphischen Tabelle von Deutschland 2016: kontinuierliche oder lückenhafte Überlieferung? The Keuper Group in the Stratigraphic Table of Germany 2016: a continuous or discontinuous stratigraphic record? *Zeitschrift der Deutschen Gesellschaft für Geowissenschaften*, **169**, 181–201. https://doi.org/10.1127/zdgg/2017/0129.

Nordt, L., **Atchley, S.** and **Dworkin, S.** (2015) Collapse of the Late Triassic megamonsoon in western equatorial Pangea, present-day American Southwest. *GSA Bulletin*, **127**, 1798–1815.

Ogg, J.G. (2015) The mysterious Mid-Carnian "Wet Intermezzo" global event. *J. Earth Sci.*, **26**, 181–191.

Olsen, P.E. (1986) A 40-million-year lake record of early Mesozoic orbital climatic forcing. *Science*, **234**, 842–848.

Olsen, P.E. and **Kent, D.V.** (1996) Milankovitch climate forcing in the tropics of Pangaea during the Late Triassic. *Palaeogeogr. Palaeoclimatol. Palaeoecol.*, **122**, 1–26.

Olsen, P.E. and **Kent, D.V.** (1999) Long-period Milankovitch cycles from the Late Triassic and Early Jurassic of eastern North America and their implications for the calibration of the Early Mesozoic time–scale and the long–term behaviour of the planets. *Philos. Trans. R. Soc. London A.*, **357**, 1761–1786.

Olsen, P.E., **Geissman, J.W.**, **Kent, D.V.**, **Gehrels, G.E.**, **Mundil, R.**, **Irmis, R.**, **Lepre, C.**, **Rasmussen, C.**, **Giesler, D.** and **Parker, W.G.** (2018) Colorado Plateau Coring Project, Phase I (CPCP-I): a continuously cored, globally exportable chronology of Triassic continental environmental change from western North America. *Scientific Drilling*, **24**, 15–40.

Olsen, P.E., **Laskar, J.**, **Kent, D.V.**, **Kinney, S.T.**, **Reynolds, D.J.**, **Sha, J.** and **Whiteside, J.H.** (2019) Mapping Solar System chaos with the Geological Orrery. *Proc. Natl Acad. Sci. USA*, **116**, 10664–10673. https://doi.org/10.1073/pnas.1813901116

Pälike, H., **Norris, R.D.**, **Herrle, J.O.**, **Wilson, P.A.**, **Coxall, H.K.**, **Lear, C.H.**, **Shackleton, N.J.**, **Tripati, A.K.** and **Wade, B.S.** (2006) The heartbeat of the oligocene climate system. *Science*, **314**, 1894–1898.

Parrish, J.T. (1993) Climate of the supercontinent Pangea. *J. Geol.*, **101**, 215–233.

Parrish, J.T. and **Peterson, F.** (1988) Wind directions predicted from global circulation models and wind directions determined from eolian sandstones of the western United States—A comparison. *Sed. Geol.*, **56**, 261–282.

Pimentel, N.L., **Wright, V.P.** and **Azevedo, T.M.** (1996) Distinguishing early groundwater alteration effects from pedogenesis in ancient alluvial basins: examples from the Palaeogene of southern Portugal. *Sed. Geol.*, **105**, 1–10.

Piper, D.J. and **Hundert, T.** (2002) Provenance of distal Sohm Abyssal Plain sediments: history of supply from the Wisconsinan glaciation in eastern Canada. *Geo-Mar. Lett.*, **22**, 75–85.

Preto, N., **Kustatscher, E.** and **Wignall, P.B.** (2010) Triassic climates — State of the art and perspectives. *Palaeogeogr. Palaeoclimatol. Palaeoecol.*, **290**, 1–10.

R Core Team (2013) *R: A Language and Environment for Statistical Computing*. R Foundation for Statistical Computing, Vienna, Austria. http://www.R-project.org/

Reinhardt, L. (2000) *Dynamic Stratigraphy and Geochemistry of the Steinmergel-Keuper playa System: A Record of Pangean Megamonsoon (Triassic, Middle Keuper, S. Germany)*. PhD, Universität Köln, Cologne, Germany, 183 pp.

Reinhardt, L. and **Ricken, W.** (1999) Climate cycles documented in a playa system: comparison of geochemical signatures derived from subbasins (Triassic, Middle Keuper, German Basin). *Zbl. Geol. Paläontol. Teil I*, **3-4**, 315–340.

Reinhardt, L. and **Ricken, W.** (2000) The stratigraphic and geochemical record of Playa Cycles: monitoring a Pangaean monsoon-like system (Triassic, Middle Keuper, S. Germany). *Palaeogeogr. Palaeoclimatol. Palaeoecol.*, **161**, 205–227.

Retallack, G.J. (2002) Carbon dioxide and climate over the past 300 Myr. *Philos Trans R Soc London A*, **360**, 659–673.

Robinson, P.L. (1973) Palaeoclimatology and continental drift. In: *Implications of Continental Drift to the Earth Sciences*, Vol. **1** (Eds D.H. Tarling and S.K. Runcorn), pp. 451–476. Academic Press, London.

Roghi, G., **Gianolla, P.**, **Minarelli, L.**, **Pilati, C.** and **Preto, N.** (2010) Palynological correlation of Carnian humid pulses throughout western Tethys. *Palaeogeogr. Palaeoclimatol. Palaeoecol.*, **290**, 89–106.

Rosen, M.R. and **Warren, J.K.** (1990) The origin and significance of groundwater-seepage gypsum from Bristol Dry Lake, California, USA. *Sedimentology*, **37**, 983–996.

Scotese, C.R. (2004) A continental drift flipbook. *J. Geol.*, **112**, 729–741.

Sellwood, B.W. and **Valdes, P.J.** (2006) Mesozoic climates: General circulation models and the rock record. *Sed. Geol.*, **190**, 269–287.

Sha, J., **Olsen, P.E.**, **Pan, Y.**, **Xu, D.**, **Wang, Y.**, **Zhang, X.**, **Yao, X.** and **Vajda, V.** (2015) Triassic–Jurassic climate in continental high-latitude Asia was dominated by obliquity-paced variations (Junggar Basin, Ürümqi, China). *Proc. Natl Acad. Sci. USA*, **112**, 3624–3629.

Stefani, M., **Furin, S.** and **Gianolla, P.** (2010) The changing climate framework and depositional dynamics of Triassic carbonate platforms from the Dolomites. *Palaeogeogr. Palaeoclimatol. Palaeoecol.*, **290**, 43–57.

Sun, J. and **Huang, X.** (2006) Half-precessional cycles recorded in Chinese loess: response to low-latitude insolation forcing during the Last Interglaciation. *Quatern. Sci. Rev.*, **25**, 1065–1072.

Sun, Y.D., **Wignall, P.B.**, **Joachimski, M.M.**, **Bond, D.P.G.**, **Grasby, S.E.**, **Lai, X.L.**, **Wang, L.N.**, **Zhang, Z.T.** and **Sun, S.** (2016) Climate warming, euxinia and carbon isotope perturbations during the Carnian (Triassic) Crisis in South China. *Earth Planet. Sci. Lett.*, **444**, 88–100.

Szurlies, M. (2004) Magnetostratigraphy: the key to a global correlation of the classic Germanic Trias-case study Volpriehausen Formation (Middle Buntsandstein), Central Germany. *Earth Planet. Sci. Lett.*, **227**, 395–410.

Szurlies, M. (2007) Latest Permian to Middle Triassic cyclomagnetostratigraphy from the Central European Basin, Germany: Implications for the geomagnetic polarity timescale. *Earth Planet. Sci. Lett.*, **261**, 602–619.

Talbot, M., **Holm, K.** and **Williams, M.** (1994) Sedimentation in low-gradient desert margin systems: A comparison of the Late Triassic of northwest Somerset (England) and the late Quaternary of east-central Australia. *Geol. Soc. Am. Spec. Paper*, **289**, 97–117.

Tanner, L.H. (2010) Cyclostratigraphic record of the Triassic: a critical examination. *Geological Society, London, Special Publications*, **334**, 119–137.

Tanner, L.H. (2018) Climates of the Late Triassic: perspectives, proxies and problems. In: *The Late Triassic World* (Ed. L.H. Tanner), pp. 59–90. Springer, Heidelberg.

Tanner, L.H. and **Lucas, S.G.** (2015) The Triassic-Jurassic strata of the Newark Basin, USA: a complete and accurate astronomically-tuned timescale? *Stratigraphy*, **12**, 47–65.

Tanner, L.H., **Hubert, J.F.**, **Coffey, B.P.** and **McInerney, D.P.** (2001) Stability of atmospheric CO_2 levels across the Triassic/Jurassic boundary. *Nature*, **411**, 675–677.

Tanner, L.H., **Lucas, S.**, **Semken, S.**, **Berglof, W.** and **Ulmer-Scholle, D.** (2003) Pedogenic features of the Chinle Group, Four Corners region: evidence of Late Triassic aridification. *New Mexico Geol. Soc. Guidebook*, **54**, 269–280.

Verschuren, D., **Sinninghe Damste, J.S.**, **Moernaut, J.**, **Kristen, I.**, **Blaauw, M.**, **Fagot, M.** and **Haug, G.H.** (2009) Half-precessional dynamics of monsoon rainfall near the East African Equator. *Nature*, **462**, 637–641.

Voigt, S., **Weber, Y.**, **Frisch, K.**, **Bartenstein, A.**, **Hellwig, A.**, **Petschick, R.**, **Bahr, A.**, **Pross, J.**, **Koutsodendris, A.** and **Voigt, T.** (2017) Climatically forced moisture supply, sediment flux and pedogenesis in Miocene mudflat deposits of south-east Kazakhstan, Central Asia. *Deposit. Rec.*, **3**, 209–232.

Vollmer, T. (2005) *Paleoclimatology of Upper Triassic Playa Cycles. New Insights Into an Orbital Controlled Monsoon System (Norian, German Basin)*, PhD, Universität zu Köln, Cologne, Germany, 164 pp.

Vollmer, T., **Werner, R.**, **Weber, M.**, **Tougiannidis, N.**, **Röhling, H.-G.** and **Hambach, U.** (2008) Orbital control on Upper Triassic Playa cycles of the Steinmergel-Keuper (Norian): a new concept for ancient playa cycles. *Palaeogeogr. Palaeoclimatol. Palaeoecol.*, **267**, 1–16.

Wang, P. (2009) Global monsoon in a geological perspective. *Chin. Sci. Bull.*, **54**, 1113–1136.

Wang, P., **Tian, J.** and **Lourens, L.J.** (2010) Obscuring of long eccentricity cyclicity in Pleistocene oceanic carbon isotope records. *Earth Planet. Sci. Lett.*, **290**, 319–330.

Wang, P.X., **Wang, B.**, **Cheng, H.**, **Fasullo, J.**, **Guo, Z.**, **Kiefer, T.** and **Liu, Z.** (2017) The global monsoon across time scales: Mechanisms and outstanding issues. *Earth Sci. Rev.*, **174**, 84–121.

Weber, M., **Tougiannidis, N.**, **Kleineder, M.**, **Bertram, N.**, **Ricken, W.**, **Rolf, C.**, **Reinsch, T.** and **Antoniadis, P.** (2010) Lacustrine sediments document millennial-scale climate variability in northern Greece prior to the onset of the northern hemisphere glaciation. *Palaeogeogr. Palaeoclimatol. Palaeoecol.*, **291**, 360–370.

Wu, H., **Zhang, S.**, **Feng, Q.**, **Jiang, G.**, **Li, H.** and **Yang, T.** (2012) Milankovitch and sub-Milankovitch cycles of the early Triassic Daye Formation, South China and their geochronological and paleoclimatic implications. *Gondwana Res.*, **22**, 748–759.

Zhang, Y.G., **Ji, J.**, **Balsam, W.L.**, **Liu, L.** and **Chen, J.** (2007) High resolution hematite and goethite records from ODP 1143, South China Sea: Co-evolution of monsoonal precipitation and El Niño over the past 600,000 years. *Earth Planet. Sci. Lett.*, **264**, 136–150.

Zhang, Y., **Li, M.**, **Ogg, J.G.**, **Montgomery, P.**, **Huang, C.**, **Chen, Z.-Q.**, **Shi, Z.**, **Enos, P.** and **Lehrmann, D.J.** (2015) Cycle-calibrated magnetostratigraphy of middle Carnian from South China: Implications for Late Triassic time scale and termination of the Yangtze Platform. *Palaeogeogr. Palaeoclimatol. Palaeoecol.*, **436**, 135–166.

Ziegler, P.A. (1990) *Geological Atlas of Western and Central Europe*. Geological Society of London, London, 256 pp.

Manuscript received 29 April 2019; revision accepted 26 September 2019

Supporting Information

Additional information may be found in the online version of this article:

Appendix S1. Spectrophotometric data obtained on the Hohenhaslach outcrop.